SUGISAKA MASANORI

Journal of Robotics, Networking and Artificial Life
Vol. 9(4); March (2023), pp. 349–357
ISSN (Online):2352-6386; ISSN (Print):2405-9021
https://alife-robotics.org/jrnal.html

Research Article

Fall Risk Estimation for Visually Impaired using iPhone with LiDAR

Daigo Katayama[1], Kazuo Ishii[1], Shinsuke Yasukawa[1], Yuya Nishida[1], Satoshi Nakadomari[2], Koichi Wada[2], Akane Befu[2], Chikako Yamada[2]

[1]*Graduate School of Life Science and Systems Engineering, Kyushu Institute of Technology, 2-4 Hibikino, Wakamatsu-ku, Kitakyushu-shi, Fukuoka, 808-0196, Japan*
[2]*NEXT VISION, Kobe Eye Center 2F, 2-1-8, Minatojima-Minamimachi, Chuo-ku, Kobe-shi, Hyogo, 650-0047, Japan*

ARTICLE INFO

Article History
Received 25 November 2021
Accepted 04 May 2023

Keywords
Electronic travel aids
Negative obstacle detection
Point cloud
LiDAR sensor

ABSTRACT

We have developed a fall risk alert system using a smartphone with a LiDAR sensor, Apple's iPhone 12 Pro, as an electronic travel aid (ETA) for visually impaired to reduce fall risks from the edge of station platform and the stairs. The proposed system generates the height grid map generated from 3D point clouds and posture from the smartphone, and classify the walking area to four areas, walkable, positive obstacle, negative obstacle and occlusion areas. In this paper, we describe the algorithm and the experimental results of the environmental recognition system for the fall risk alert. In the experiments, the accuracy, stability, and time delay are evaluated in approaching a fall risk area, such as stairs. The results show the smartphone has the possibility to be the ETA to support the visually impaired and reduce the fall risks.

1. Introduction

Fall accidents on station platforms are one of severe problems for the visually impaired during walk alone. According to statistics data from the Ministry of Land, Infrastructure, Transport, and Tourism in Japan [1], the average of approximately 76 fall accidents occurs every year. One of factors of the fall accidents is the difficulty for the visually impaired to recognize road conditions further away than detecting with a cane (until approx. 1 m ahead), and they don't have enough time to find and avoid obstacles with their walking speed [2]. To reduce the fall accidents, the visually impaired needs to identify areas likely to fall down including further area than notified area with a cane. To solve this problem, the support devices called Electronic Travel Aids (ETAs) have been developed, which inform alert using ultrasonic or infrared sensors to the visually impaired in non-visual information formats such as sound and vibration [3]. In recent years, a lot of research and development have been done on ETAs which detect and emit a warning of entering fall risk areas, such as stairs and gaps. However, the primary purpose of commercially available ETAs such as Miniguide [4], UltraCane [5], WeWALK [6], Sunu band [7], BuzzClip [8] are positive obstacle detection (walls, pillars, etc.) and warn approaching obstacles. Few devices device have been commercialized to make a warning on approaching of fall risk areas. Due to the development of information technology and computers, smartphones with high computational power and sensors are available and widespread recently. Smartphones have the big possibility to be the supporting tools for the visually impaired as the smartphones have necessary functions such as voice recognition, image processing, GPS positioning and navigation, internet services, LiDAR and so on.

In this research, an ETA, whose main component is a smartphone with LiDAR sensor, has been proposed and evaluated. The ETA obtains the distance data of surroundings using the LiDAR sensor and estimate the fall

Corresponding author's E-mail: katayama.daigo696@mail.kyutech.jp, ishii@brain.kyutech.ac.jp, s-yasukawa@brain.kyutech.ac.jp, y-nishida@brain.kyutech.ac.jp, satoshin1@mac.com, wakichi@nextvision.or.jp, befu@nextvision.or.jp, yamada@nextvision.or.jp
URL: www.lsse.kyutech.ac.jp

risk of walking area, and labels the risk level. The algorithm of ETA is proposed and evaluated through experiments.

2. Related Works

2.1. *Electronic Travel Aids to Make Warning of Fall Risk*

Most of commercially available ETAs alert their users for the fall risk based on the distances to the walking floor. The distance to the floor in the earth coordinate is calculated using 3D posture information from the IMU sensor, and make a warning if the distance to the floor exceeds the threshold value. The ETAs have the appearance of a wearable device, such as a belt type [9], [10], a cart type [11], a cane-integrated type [12], [13], [14] and a headgear type [15], [16]. Also, negative obstacle detection algorithms for the ETAs have been developed: the edge detection from stereo vision using seed growing and dynamic programming [17], the staircase detection using image processing and support vector machine (SVM) from RGB and depth (RGB-D) images [18] and the ground and hole detection from disparity image [19]. Many ETAs and algorithms have been developed, however, few devices have achieved the commercialization process.

2.2. *Smartphone-based Electronic Travel Aids*

The smartphones consist of computers, cameras, IMU, GPS and so on, and also many advanced applications have been implemented on them for the visually impaired. For examples, Seeing AI [20] (Microsoft Corp.) and Envision AI [21] (Envision Technologies B.V.) were already available as commercial applications for object recognition and notification of recognition results. High-end models of Apple's smartphones after iPhone 12 Pro have a LiDAR sensor [22] which enables iPhone to acquire high accuracy and wide range of distance information to the surroundings and is often used for navigation by combining the distance information, IMU data, heading, height and GPS position. For examples, those applications offer the functions such as the guidance on aisles [23], recognition to assist in following a line [24], positive obstacle detection and intersection detection for indoor walking assistance [25].

3. Fall Risk Estimation Method

3.1. *Basic Concept*

We have developed an ETA using a smartphone with LiDAR to inform the fall risk areas ahead of the visually impaired where he/she cannot recognize with a cane as shown in Fig. 1, and offers safety checks in advance to reach those area if used with the cane. We assume that the ETA (iPhone) is attached on the user's chest with a tilt downwards to measure the distances of walking surface. The ETA estimates the surface height and compare with current ground level, and the height is not within the safety region, ETA vibrates and the connected smart watch also make alarms and vibrations. As shown in Fig. 2, the ETA categorizes the front surface to four areas, positive obstacle area (blue), walkable area (green), negative obstacle area (orange) and occlusion area (red) based on the surface height ${}^{\mathrm{R}}z_{\mathrm{R}}$ in coordinate Σ_{R} whose z-axis is in the gravity direction. The coordinate Σ_{C} is the local coordinate corresponding to the ETA. Comparing the surface height with that of ETA H_{chest}, system determines the category of front surface. Here, X_{min} is the distance to the nearest line of mapping area of the recognition space to the ground surface, X_{max} is that of the farest line, x_{edge} is that of the nearest mesh of occlusion or negative obstacle areas. X_{th1}, X_{th2}, X_{th3} are distance thresholds for the fall risk estimation.

3.2. *Algorithm of Fall Risk Estimation*

The flow of the algorithm for fall risk estimation is shown in Fig. 3, and the area s_{risk} of the fall risk area at the recognition space. The details of the process in each step are shown below.

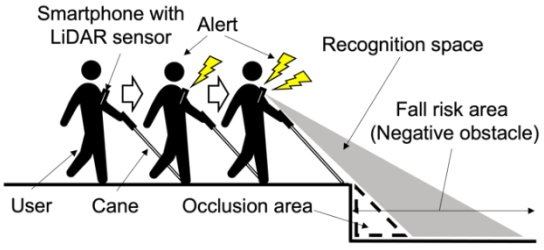

Fig. 1 Concept of electronic travel aid

(1) Generate Point Cloud

A 3D point ${}^{\mathrm{C}}\boldsymbol{p} = [\,{}^{\mathrm{C}}x_{\mathrm{C}},\ {}^{\mathrm{C}}y_{\mathrm{C}},\ {}^{\mathrm{C}}z_{\mathrm{C}}]^T \in \Sigma_{\mathrm{C}}$ (Camera coordinate) is calculated from the depth d_{uv} [26] from the LiDAR sensor and ${}^{\mathrm{P}}u$, ${}^{\mathrm{P}}v$, which are in the coordinates on the depth image plane Σ_{P}, c_u and c_v are the center position on Σ_{P}, f_u and f_v are the focus parameters, as shown in Eq. (1).

$$ {}^{\mathrm{C}}\boldsymbol{p} = \begin{bmatrix} {}^{\mathrm{C}}x_{\mathrm{C}} \\ {}^{\mathrm{C}}y_{\mathrm{C}} \\ {}^{\mathrm{C}}z_{\mathrm{C}} \end{bmatrix} = \begin{bmatrix} \dfrac{{}^{\mathrm{P}}u - c_u}{f_u} \\ \dfrac{{}^{\mathrm{P}}v - c_v}{f_v} \\ 1 \end{bmatrix} d_{uv} \tag{1} $$

The point ${}^{\mathrm{C}}\boldsymbol{p}$ is transformed from Σ_{C} to Σ_{R}(Recognition space coordinate). ${}^{\mathrm{R}}\boldsymbol{p} = [\,{}^{\mathrm{R}}x_{\mathrm{R}},\ {}^{\mathrm{R}}y_{\mathrm{R}},\ {}^{\mathrm{R}}z_{\mathrm{R}}]^T \in \Sigma_{\mathrm{R}}$ by using gravity direction from IMU. In the coordinate transformation, the quaternion ${}^{\mathrm{C}'}\tilde{q}$, ${}^{\mathrm{R}}\tilde{q}$, ${}^{\mathrm{C}'}\tilde{q}^*$ and ${}^{\mathrm{R}}\tilde{q}^*$. ${}^{\mathrm{C}'}\tilde{q}$ are used for the calculation of the coordinate transformation. ${}^{\mathrm{R}}\tilde{q}$ is obtained from the smartphone's 3D posture on Σ_{R}. ${}^{\mathrm{C}'}\tilde{q}$ and ${}^{\mathrm{R}}\tilde{q}$ are defined as shown in Eq. (2) and Eq. (3), respectively.

$$ {}^{\mathrm{C}'}\tilde{q} = {}^{\mathrm{C}'}q_w + {}^{\mathrm{C}'}q_x\boldsymbol{i}' + {}^{\mathrm{C}'}q_y\boldsymbol{j}' + {}^{\mathrm{C}'}q_z\boldsymbol{k}' = {}^{\mathrm{C}'}q_w + {}^{\mathrm{C}'}\boldsymbol{q} \tag{2} $$

$$ {}^{\mathrm{R}}\tilde{q} = {}^{\mathrm{R}}q_w + {}^{\mathrm{R}}q_x\boldsymbol{i} + {}^{\mathrm{R}}q_y\boldsymbol{j} + {}^{\mathrm{R}}q_z\boldsymbol{k} = {}^{\mathrm{R}}q_w + {}^{\mathrm{R}}\boldsymbol{q} \tag{3} $$

${}^{\mathrm{C}'}q_w$, ${}^{\mathrm{C}'}q_x$, ${}^{\mathrm{C}'}q_y$ and ${}^{\mathrm{C}'}q_z$ are scalar values on $\Sigma_{\mathrm{C}'}$, whose unit vectors are $\boldsymbol{i}'$, $\boldsymbol{j}'$, and $\boldsymbol{k}'$, and ${}^{\mathrm{R}}q_w$, ${}^{\mathrm{R}}q_x$, ${}^{\mathrm{R}}q_y$ and ${}^{\mathrm{R}}q_z$ are on Σ_{R} whose unit vectors are $\boldsymbol{i}$, $\boldsymbol{j}$, and $\boldsymbol{k}$.

${}^{\mathrm{C}'}\tilde{q}^*$ and ${}^{\mathrm{R}}\tilde{q}^*$ are the conjugate quaternions of ${}^{\mathrm{C}'}\tilde{q}$ and ${}^{\mathrm{R}}\tilde{q}$, respectively. The coordinate transformed point ${}^{\mathrm{C}'}\boldsymbol{p} = [\,{}^{\mathrm{C}'}x_{\mathrm{C}'},\ {}^{\mathrm{C}'}y_{\mathrm{C}'},\ {}^{\mathrm{C}'}z_{\mathrm{C}'}]^T \in \Sigma_{\mathrm{C}'}$ is obtained from Eq. (4), and ${}^{\mathrm{R}}\boldsymbol{p}$ is obtained from Eq. (5).

$$ {}^{\mathrm{C}'}\boldsymbol{p} = {}^{\mathrm{C}'}\tilde{q}^*\ {}^{\mathrm{C}}\boldsymbol{p}\ {}^{\mathrm{C}'}\tilde{q} \tag{4} $$

$$ {}^{\mathrm{R}}\boldsymbol{p} = {}^{\mathrm{R}}\tilde{q}^*\ {}^{\mathrm{C}'}\boldsymbol{p}\ {}^{\mathrm{R}}\tilde{q} \tag{5} $$

(2) Generate Grid Map

Using the point ${}^{\mathrm{R}}\boldsymbol{p}$, the grid map is generated to reduce the noise in the points and simplify the calculation. The height $\overline{{}^{\mathrm{R}}z_{\mathrm{R}}}$ in each grid is calculated as the average of z-axis position in the points ${}^{\mathrm{R}}\boldsymbol{p}_{mn}$ in each grid, defined in Eq. (6). M and N are the lengths of each axis on the grid map, $m = 0, 1, \ldots, M-1$ and $n = 0, 1, \ldots, N-1$ are position on Σ_{M}(grid map coordinate), $X_{\min}$ and $Y_{\min}$ are minimum value of ${}^{\mathrm{R}}x_{\mathrm{R}}$ and ${}^{\mathrm{R}}y_{\mathrm{R}}$ on grid map, respectively. $D_{\max}$ is maximum depth on the depth image.

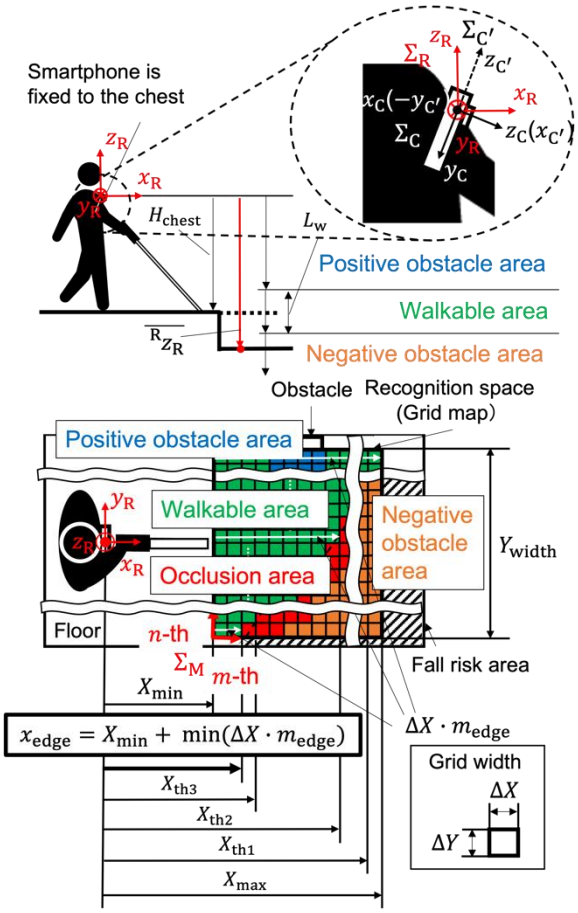

Fig. 2 Classification of front ground into four areas

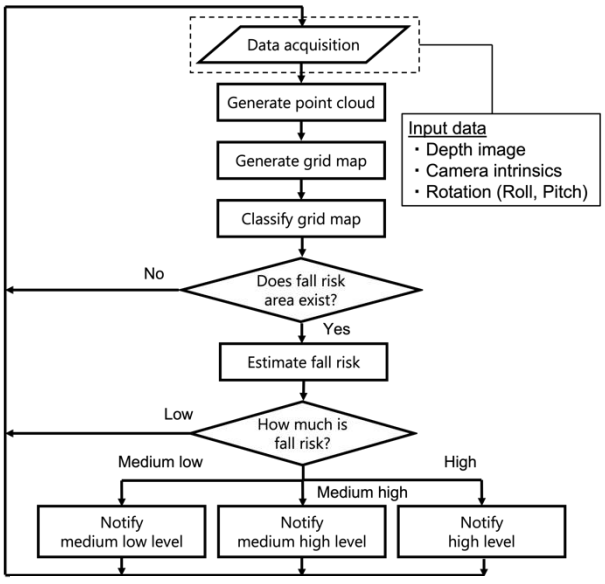

Fig. 3 Flowchart of fall risk estimation

$$
{}^{\mathrm{R}}\boldsymbol{p}_{mn} \in \left\{ {}^{\mathrm{R}}\boldsymbol{p} \;\middle|\; \begin{array}{c} m\Delta X + X_{\min} \le {}^{\mathrm{R}}x_{\mathrm{R}} < (m+1)\Delta X + X_{\min}, \\ n\Delta Y + Y_{\min} \le {}^{\mathrm{R}}y_{\mathrm{R}} < (n+1)\Delta Y + Y_{\min}, \\ -D_{\max} \le {}^{\mathrm{R}}z_{\mathrm{R}} \le D_{\max} \end{array} \right\} \quad (6)
$$

$\overline{{}^{\mathrm{R}}z_{\mathrm{R}}}$ is calculated as shown in Eq. (7). n_p is the number of ${}^{\mathrm{R}}\boldsymbol{p}_{mn}$.

$$
\overline{{}^{\mathrm{R}}z_{\mathrm{R}}} = (1/n_p) \cdot \sum_{{}^{\mathrm{R}}z_{\mathrm{R}} \in {}^{\mathrm{R}}\boldsymbol{p}_{mn}} {}^{\mathrm{R}}z_{\mathrm{R}} \quad (7)
$$

(3) Classify Grid Map

The system classifies each cell in the grid map by thresholds areas into four labels, walkable area(A_1), positive obstacle area(A_2), negative obstacle area(A_3), and occlusion area(A_4). Equation (8) provides classification of $A\left(n_p, \overline{{}^{\mathrm{R}}z_{\mathrm{R}}}\right)$ using the parameters, n_p and $\overline{{}^{R}z_{\mathrm{R}}}$.

$$
A\left(n_p, \overline{{}^{\mathrm{R}}z_{\mathrm{R}}}\right) = \begin{cases} A_1 \left(\text{if } n_p \neq 0, H_{\text{chest}} - \dfrac{L_{\mathrm{w}}}{2} \le \overline{{}^{\mathrm{R}}z_{\mathrm{R}}} \le H_{\text{chest}} + \dfrac{L_{\mathrm{w}}}{2}\right) \\ A_2 \left(\text{if } n_p \neq 0, \overline{{}^{\mathrm{R}}z_{\mathrm{R}}} > H_{\text{chest}} + \dfrac{L_{\mathrm{w}}}{2}\right) \\ A_3 \left(\text{if } n_p \neq 0, \overline{{}^{\mathrm{R}}z_{\mathrm{R}}} < H_{\text{chest}} - \dfrac{L_{\mathrm{w}}}{2}\right) \\ A_4 \left(\text{if } n_p = 0\right) \end{cases} \quad (8)
$$

(4) Estimate Fall Risk

The fall risk is estimated, the classified cells along x-axis direction in the grid map, and the edge position on each row of the grid map m_{edge} is defined as the edge cell where label of $A\left(n_p, \overline{{}^{\mathrm{R}}z_{\mathrm{R}}}\right)$ changes from walkable area (A_1) to fall risk area (A_3 or A_4). The minimum distance from the edge x_{edge} is calculated by Eq. (9) to the row with the minimum number of cells to the edge. ΔX is the grid width.

$$
x_{\text{edge}} = X_{\min} + \Delta X \cdot \min\left(m_{\text{edge}}\right) \quad (9)
$$

Next step, this system calculates the size of the fall risk area s_{risk} by Eq. (10). n_{risk} is the number of cells classified into Occlusion area or Negative obstacle area. N_{grid} is total number of cells.

$$
s_{\text{risk}} = n_{\text{risk}} \,/\, N_{\text{grid}} \quad (10)
$$

As the final step, the fall risk level FR is calculated by x_{edge} and s_{risk} as shown in Fig. 4. The level is classified into 4 levels (0,1,2,3) as shown below. X_{th1} and X_{th2}, and X_{th3} are distance thresholds ($X_{\text{th1}} > X_{\text{th2}} > X_{\text{th3}}$). S_{th} is area threshold of fall risk area.

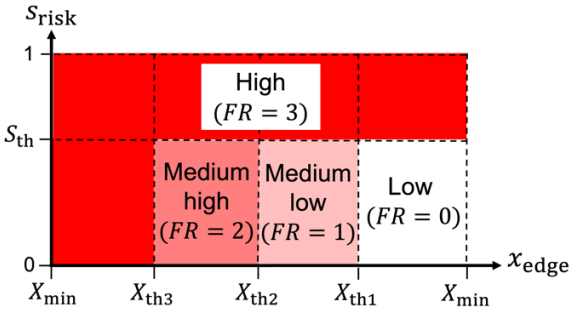

Fig. 4 Definition of fall risk level

3.3. *Algorithm Implementation into Smartphone*

The fall risk estimation algorithm describe in the previous section was implemented as the iOS app for travel aids for visually impaired. The GUI of the application is shown in Fig. 5. The grid map preview in the center is the top view with the bottom side as the user side. H_{chest} and H_{w} settings and start/end of data recording can be operated in the control panel.

The simulator was created to consider the appropriate parameters in this algorithm using MATLAB R2022a. The simulation results in the top view of the grid map, color-coded by area, as shown in Fig. 6.

3.4. *Experiments at Fall Risk Area*

Two kinds of experiments to approach a fall risk area were conducted to compare the transition of labeling by changing the approach angles into the fall risk area, the accuracy of the minimum distance estimation, and the responsiveness of the notification as follows.

(1) Procedure

The task of the experiments is that the subject with the device on the chest walks straight to the stairs, as shown in Fig. 7. The approach angle θ_a are (i) 90[deg] and (ii) 45[deg]. Here, subject was a sighted person, and the experiment was conducted without a blindfold for safety reasons.

Condition (i) assumed that user is getting on the train, and condition (ii) is moving along the platform and approaching the edge of the platform. Also, the length l_0 from subject to fall risk area was 3[m]. The collected data during the experiment were depth images, attitudes, and self-position from smartphone.

The smartphone was fixed to the front of the subject's chest with a harness-type fixture. The smartphone was also tilted downward 30[deg].

This experiment was done on the outdoor at the Wakamatsu campus of Kyushu Institute of Technology. As shown in Fig. 8, the space has wide stairs with the height of step 0.14[m] and the length 0.34[m].

(2) Analysis Method

The accuracy, stability, and delay of the fall risk estimation are evaluated by using the data recorded in this experiment to calculate the fall risk using the algorithm proposed here and comparing the fall risk at each time with each parameter used in the calculation. In the analysis, H_{chest} = 1.32[m], X_{th1} = 2.35[m], X_{th2} =1.85[m], X_{th3} = 1.35[m], S_{th} = 0.5, Y_{width} = 1.00[m], and H_{w} = 0.10[m]. The grid width ΔX and ΔY were 0.05[m] in x and y-axis directions.

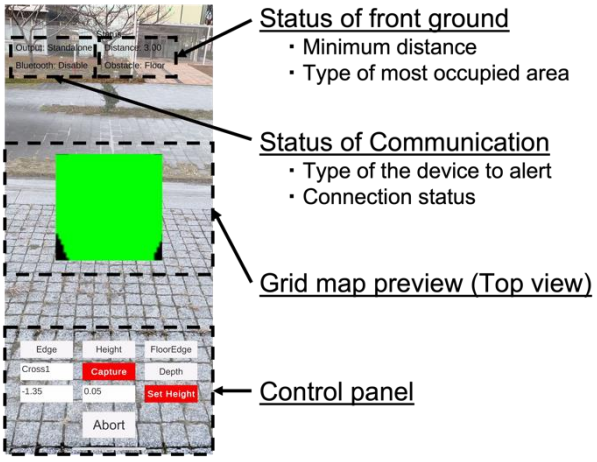

Fig. 5 Overview of App GUI

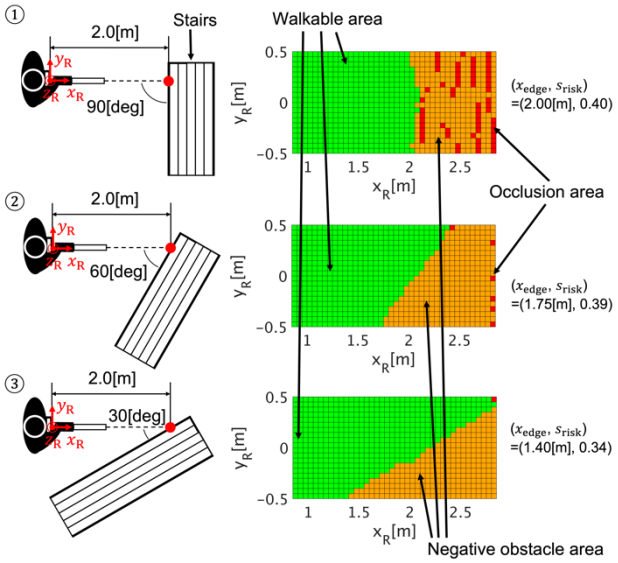

Fig. 6 Examples of grid map simulations

(3) Results

The minimum distance, fall risk area, and the fall risk level for the approach angle of 90[deg] is shown in Fig. 9 and for an approach angle of 45[deg] in Fig. 10. In all cases, the fall risk level increased in steps as one approached the fall risk area. Figure 11 shows the results of the grid map transition. At first, the area is green to show safety area, and as going to stairs, the red (occlusion) and orange (negative obstacle) areas appear in front of the subject. In the case of 45[deg] approach, the orange area appears from right side of subject as we expected.

4. Discussions

4.1. *Discussion on Approach Angle*

The results of approaches with the angles of 90[deg] and 45[deg] show that the trends are similar except for the span of the level increase. This result indicates the possibility to be robust system on approaching angles. However, the result shows the difference in the timing to

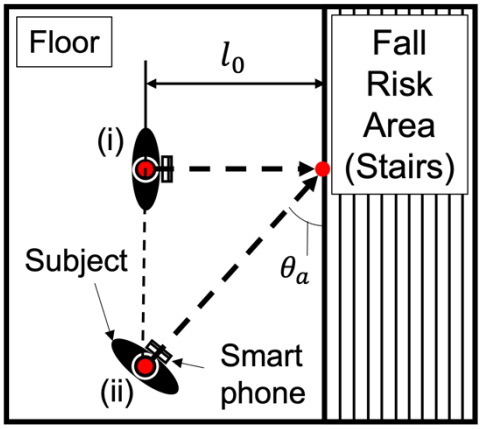

Fig. 7 Experiment conditions

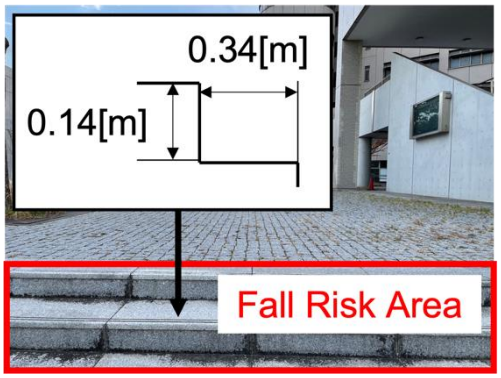

Fig. 8 Experiment site with stairs

change to the maximum fall risk level. In the case of 90[deg], the time duration of the fall risk level changes from 2 to 3 is 0.02～0.20[s]. The fall risk area increases at a faster rate than the case of 45[deg] approach. Also, focusing on x_{edge} and s_{risk} in Fig. 6, the example indicates that x_{edge} becomes shorter (2.00[m] to 1.40[m]) as θ_a decreases with the same distance from the fall risk area. For maximum fall risk estimation, s_{risk} may be dominant when θ_a increases and x_{edge} may be dominant when θ_a decreases. Therefore, X_{th1} to X_{th3} and S_{th} need to be set with considering the approaching angle θ_a.

4.2. *Discussion on Fall Risk Estimation*

We discuss the fall risk estimation algorithm, stability, and delay, considering the case of visually impaired users of this system based on the analysis result.

(1) Accuracy of Fall Risk Estimation

In the experiment, the risk level had changed as we expected. However, the variation of walking environment should be considered into the set of parameters for the fall risk estimation. The experiments were conducted in an environment with relatively small gaps around stairs, so that we should conduct a lot of experiments with various gaps, such as at the edge of a station platform. Then it needs to carry out experiments with visually impaired subjects to evaluate whether this fall risk level is adequately communicated to the visually impaired and notification of this level will help improve safety confirmation techniques.

(2) Stability of Fall Risk Estimation

The fall risk estimation results are stable except around the minimum distance threshold based on the analysis results of this experiment. This result indicates that the fall risk notification is stable for situations other than near the threshold of the minimum distance. The algorithm will reduce the confusion of the visually impaired by notification. A hysteresis addition to the threshold would improve stability for fall risk estimation around the minimum distance threshold. Consider setting the hysteresis range based on walking speed, grid size.

(3) Delay of Fall Risk Estimation

In the analysis result, we found that the fall risk level increased when the threshold was exceeded for each of the parameters. the results indicate small delay in the algorithm concerning fall risk estimation.

Since we are considering using the smartphone's vibration function in the actual notification, the design of the notification must consider the delay that would result from using these functions.

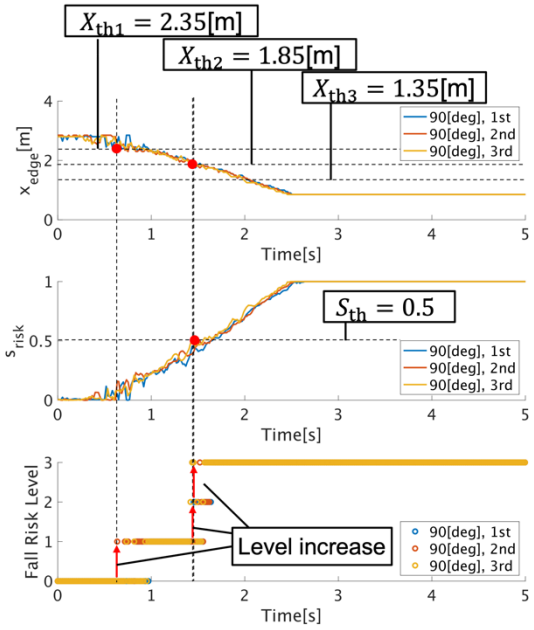

Fig. 9 Analysis results ($\boldsymbol{\theta_a}$ =90[deg])

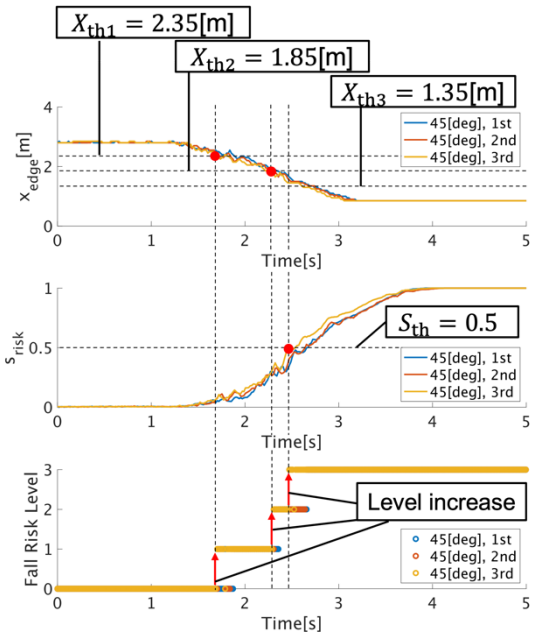

Fig. 10 Analysis results ($\boldsymbol{\theta_a}$ =45[deg])

5. Conclusion

In this paper, we proposed a fall risk estimation system for visually impaired using distance information from LiDAR sensor on the smartphone and evaluated through

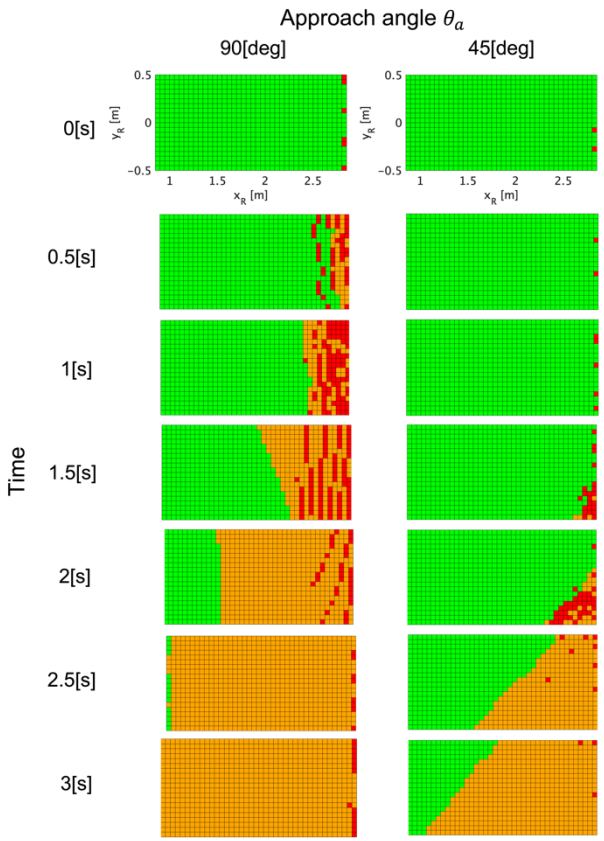

Fig. 11 Grid map simulation of experiments

experiments. The experimental results show that the system has enough possibility to estimate fall risk, which could categorize the area to four kinds of areas in the approach angle 90 and 45 degrees to the stairs, using only the information obtained from a smartphone with a LiDAR sensor. The propose algorithm was implemented as the smartphone application and could make an alert of safety confirmation for subject.

Future issues include stabilizing the fall risk estimation by adding hysteresis and examining the parameters of the fall risk estimation through evaluation experiments under actual operating conditions.

Acknowledgments

This research was supported by the Research Grant of JR–West Relief Foundation in 2020 (Grant No. 20R032).

References

1. Ministry of Land, Infrastructure and Transport, “Study Group for Improving Safety at Station Platforms”, https://www.mlit.go.jp/tetudo/tetudo_fr7_000015.html. (In Japanese, Accessed 22 Apr. 2022)
2. M. Tauchi, T. Ohkura, “A Present Situation and Problems of Independent Travel of Blind and Visual Impaired”, Journal of the Society of Instrument and Control Engineers, vol. 34, no. 2, pp. 140-146, 1995. (In Japanese)
3. T. Ohkura et al., “Science of Orientation and Mobility of Persons with Visual Impairment -Toward Safe and Reliable Independent Travel-”, CORONA PUBLISHING CO., LTD., 2014. (In Japanese)
4. GDP Research, “The Miniguide mobility aid”, http://www.gdp-research.com.au/minig_1.htm. (Accessed 22 Apr. 2022)
5. Sound Foresight Technology Ltd., “About the UltraCane”, https://www.ultracane.com/about_the_ultracane. (Accessed 22 Apr. 2022)
6. Wewalk, “The Perfect Pairing for Ultimate Visually Impaired Mobility”, https://wewalk.io/en/product/.(Accessed 22 Apr. 2022)
7. Sunu Inc., “THE SUNU BAND”, https://sunu.io/pages/sunu-band. (Accessed 15 Jan. 2023)
8. iMerciv Inc., “BuzzClip User Guide”, https://www.imerciv.com/user-guide/index.shtml. (Accessed 22 Apr. 2022)
9. R. K. Katzschmann, B. Araki, and D. Rus, “Safe Local Navigation for Visually Impaired Users With a Time-of-Flight and Haptic Feedback Device”, IEEE Transactions on Neural Systems and Rehabilitation Engineering, vol. 26, no. 3, pp. 583–593, 2018.
10. E. J. Argüello Prada and L. M. Santacruz Forero, “A belt-like assistive device for visually impaired people: Toward a more collaborative approach”, Cogent Engineering, vol. 9, no. 1, pp. 2048440, 2022.
11. C. Feltner et al., “Smart Walker for the Visually Impaired”, 2019 IEEE International Conference on Communications (ICC), pp. 1–6, 2019.
12. M. Murakami et al., “E-cane with Situation Presumption for the Blind”, Transactions of the Institute of Systems, Control and Information Engineers, vol. 16, no. 6, pp.287-294, 2003. (In Japanese)
13. N. S. Ahmad, N. L. Boon, and P. Goh, “Multi-Sensor Obstacle Detection System Via Model-Based State-Feedback Control in Smart Cane Design for the Visually Challenged”, IEEE Access, vol. 6, pp. 64182–64192, 2018.
14. M. M. Billah et al., “Experimental investigation of a novel walking stick in avoidance drop-off for visually impaired people”, Cogent Engineering, vol. 6, no. 1, pp. 1692468, 2019.
15. S. Caraiman et al., “Computer Vision for the Visually Impaired: the Sound of Vision System”, 2017 IEEE International Conference on Computer Vision Workshops (ICCVW), pp. 1480–1489, 2017.
16. M. M. Islam, M. S. Sadi, and T. Bräunl, “Automated Walking Guide to Enhance the Mobility of Visually Impaired People”, IEEE Transactions on Medical Robotics and Bionics, vol. 2, no. 3, pp. 485-496, 2020.
17. S. Fazli, H. M. Dehnavi, and P. Moallem, “A robust negative obstacle detection method using seed-growing and dynamic programming for visually-impaired/blind persons”, Optical Review, vol. 18, no. 6, pp. 415-422, 2011.

18. R. Munoz, X. Rong, and Y. Tian, "Depth-aware indoor staircase detection and recognition for the visually impaired", 2016 IEEE International Conference on Multimedia & Expo Workshops (ICMEW), pp. 1-6, 2016.
19. P. Herghelegiu, A. Burlacu, and S. Caraiman, "Negative obstacle detection for wearable assistive devices for visually impaired", 2017 21st International Conference on System Theory, Control and Computing (ICSTCC), pp. 564-570, 2017.
20. Microsoft Corp., "Seeing AI App from Microsoft", https://www.microsoft.com/en-us/ai/seeing-ai. (Accessed 24 Apr. 2022)
21. Envision Technologies B. V., "Envision App", https://www.letsenvision.com/envision-app. (Accessed 24 Apr. 2022)
22. Apple Inc., "Compare iPhone models", https://www.apple.com/iphone/compare/?modelList=iphone13pro-max,iphone13pro,iphone13. (Accessed 29 Aug. 2022)
23. V.Bharati, "LiDAR+ Camera Sensor Data Fusion On Mobiles With AI-Based Virtual Sensors To Provide Situational Awareness For The Visually Impaired.", 2021 IEEE Sensors Applications Symposium (SAS), pp. 1–6, 2021.
24. M. Kuribayashi et al., "LineChaser: A Smartphone-Based Navigation System for Blind People to Stand in Lines", Proceedings of the 2021 CHI Conference on Human Factors in Computing Systems, no. 33, pp. 1-13, 2021.
25. M. Kuribayashi et al., "Corridor-Walker: Mobile Indoor Walking Assistance for Blind People to Avoid Obstacles and Recognize Intersections", Proceedings of the ACM on Human-Computer Interaction, vol. 6, no. MHCI, pp. 1–22, 2022.
26. Y. Wang et al., "Pseudo-Lidar From Visual Depth Estimation: Bridging the Gap in 3d Object Detection for Autonomous Driving." Proceedings of the IEEE/CVF Conference on Computer Vision and Pattern Recognition (CVPR), pp. 8437-8445, 2019.
27. M. Yatabe, "Handy Note for Quaternions", MSS Technical Report, vol. 18, pp. 29-34, 2007. (In Japanese)

Appendix A. Quaternion [27]

Quaternion is defined by Eq. (A.1). q_0 is the scalar part, $\boldsymbol{q} = q_1\boldsymbol{i} + q_2\boldsymbol{j} + q_3\boldsymbol{k}$ is the vector part in the cartesian coordinate system. $\boldsymbol{i}$, $\boldsymbol{j}$, and $\boldsymbol{k}$ are basis vectors in the Cartesian coordinate system, x -axis, y -axis, and z-axis, respectively. Also, $\boldsymbol{i}, \boldsymbol{j}$, and $\boldsymbol{k}$ are provided in Eq. (A.3) from the vector product $\boldsymbol{a}$ and $\boldsymbol{b}$ defined in Eq. (A.2).

$$\tilde{q} = q_0 + \boldsymbol{q} = q_0 + q_1\boldsymbol{i} + q_2\boldsymbol{j} + q_3\boldsymbol{k} \quad (A.1)$$

$$\boldsymbol{ab} \equiv -\boldsymbol{a}\cdot\boldsymbol{b} + \boldsymbol{a}\times\boldsymbol{b} \quad (A.2)$$

$$\boldsymbol{i}^2 + \boldsymbol{j}^2 + \boldsymbol{k}^2 = \boldsymbol{ijk} = -1$$
$$\boldsymbol{ij} = -\boldsymbol{ji} = \boldsymbol{k}, \boldsymbol{jk} = -\boldsymbol{kj} = \boldsymbol{i}, \boldsymbol{ki} = -\boldsymbol{ik} = \boldsymbol{j} \quad (A.3)$$

Conjugate quaternion $\tilde{q}^*$ is the inverted sign of the vector part of the quaternion $\tilde{q}$, as shown in Eq. (A.4).

$$\tilde{q}^* = q_0 - \boldsymbol{q} = q_0 - q_1\boldsymbol{i} - q_2\boldsymbol{j} - q_3\boldsymbol{k} \quad (A.4)$$

The quaternion product of two quaternions $\tilde{q}$ and $\tilde{p} = p_0 + \boldsymbol{p} = p_0 + p_1\boldsymbol{i} + p_2\boldsymbol{j} + p_3\boldsymbol{k}$ is shown in Eq. (A.5) from Eq. (A.2). Also, the quaternion product is noncommutative ($\tilde{q}\tilde{p} \neq \tilde{p}\tilde{q}$).

$$\tilde{q}\tilde{p} = (q_0 + \boldsymbol{q})(p_0 + \boldsymbol{p}) = q_0p_0 + q_0\boldsymbol{p} + p_0\boldsymbol{q} - \boldsymbol{q}\cdot\boldsymbol{p} + \boldsymbol{q}\times\boldsymbol{p} \quad (A.5)$$

The norm of quaternions is shown as Eq. (A.6).

$$\|\tilde{q}\| = \sqrt{q_0^2 + q_1^2 + q_2^2 + q_3^2} \quad (A.6)$$

The quaternion provided the rotation is provided as Eq. (A.7). $\boldsymbol{n}$ is the unit vector in the cartesian coordinate system. θ is the rotation angle. This quaternion's norm is $\|\tilde{q}\| = 1$.

$$\tilde{q} = \cos\frac{\theta}{2} + \boldsymbol{n}\sin\frac{\theta}{2} \quad (A.7)$$

By using the quaternions in Eq. (A.7), the rotation of the position vector $\boldsymbol{r} = [x, y, z]^T$ and the rotation of the coordinate system are shown in Eq. (A.8) and Eq. (A.9), respectively.

$$\boldsymbol{r}' = \tilde{q}\boldsymbol{r}\tilde{q}^* \quad (A.8)$$

$$\boldsymbol{r}'' = \tilde{q}^*\boldsymbol{r}\tilde{q} \quad (A.9)$$

Equation (A.10) and Eq. (A.11) are expanding Eq. (A.8) and Eq. (A.9), respectively. Equation (A.10) is equal to the rotation of the position vector shown in Fig. A.1; Eq. (A.11) is the reverse order of the vector product in the third term of Eq. (A.10), which provides the rotation of the coordinate system.

$$\boldsymbol{r}' = \left(\cos\frac{\theta}{2} + \boldsymbol{n}\sin\frac{\theta}{2}\right)\boldsymbol{r}\left(\cos\frac{\theta}{2} - \boldsymbol{n}\sin\frac{\theta}{2}\right)$$
$$= (\boldsymbol{r}\cdot\boldsymbol{n})\boldsymbol{n} + \{\boldsymbol{r} - (\boldsymbol{r}\cdot\boldsymbol{n})\boldsymbol{n}\}\cos\theta + \boldsymbol{n}\times\boldsymbol{r}\sin\theta \quad (A.10)$$

$$\boldsymbol{r}'' = \left(\cos\frac{\theta}{2} - \boldsymbol{n}\sin\frac{\theta}{2}\right)\boldsymbol{r}\left(\cos\frac{\theta}{2} + \boldsymbol{n}\sin\frac{\theta}{2}\right)$$
$$= (\boldsymbol{r}\cdot\boldsymbol{n})\boldsymbol{n} + \{\boldsymbol{r} - (\boldsymbol{r}\cdot\boldsymbol{n})\boldsymbol{n}\}\cos\theta + \boldsymbol{r}\times\boldsymbol{n}\sin\theta \quad (A.11)$$

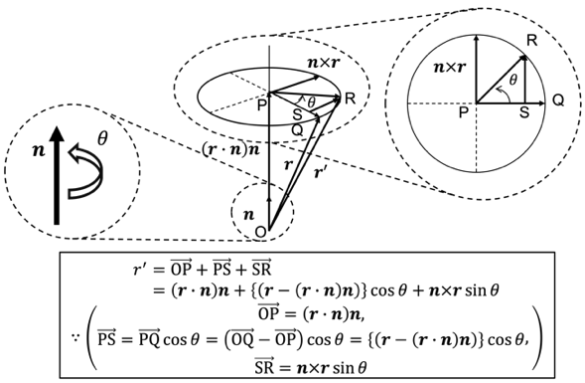

Fig. A.1 Position vector rotation
(Modified from the paper [27])

Authors Introduction

Mr. Daigo Katayama

He is a Doctoral Student at Graduate School of Life Science and Systems Engineering, Kyushu Institute of University. He received Master's degree from Graduate School of Life Science and Systems Engineering, Kyushu Institute of University.

Prof. Kazuo Ishii

He is a Professor at Graduate School of Life Science and Systems Engineering, Kyushu Institute of University. He received Ph.D. from School of Engineering, The University of Tokyo.

Dr. Shinsuke Yasukawa

He is an Associate Professor at Graduate School of Life Science and Systems Engineering, Kyushu Institute of University. He received Ph.D. from Graduate School of Engineering, Osaka University.

Dr. Yuya Nishida

He is an Associate Professor at Graduate School of Life Science and System Engineering, Kyushu Institute of Technology. He received Ph.D. from Graduate School of Life Science and Systems Engineering, Kyushu Institute of University.

Dr. Satoshi Nakadomari

He is a Director at NEXT VISION. He graduated from the Department of Medical, The Jikei University. He received Ph.D. from the Department of Medical, The Jikei University.

Mr. Koichi Wada

He is a Vision Park Information Master at NEXT VISION. He graduated from Acupuncture and Physical Therapy Teacher Training School of University of Tsukuba.

Ms. Akane Befu

She is a Vision Park Information Concierge at NEXT VISION. She graduated from The Department of Domestic Science, Tokushima Bunri University.

Ms. Chikako Yamada

She is an Executive Secretary at NEXT VISION. She graduated Graduate School of Sociology, Bukkyo University. She received Master's degree from Graduate School of Sociology, Bukkyo University.